3D-CFD analysis of the effect of cooling via minitubes on the performance of a three-fluid combined membrane contactor

Ehsan Afrasiabian[1,*], Oleg Iliev[1], Inga Shklyar[1], Torben Prill[1], Carlo Isetti[2] and Stefano Lazzari[3]

[1]*Flows and Materials Simulation Department, Fraunhofer-Institute for Industrial Mathematics (ITWM), Fraunhofer-Platz 1, 67663 Kaiserslautern, Germany;* [2]*Innovative Technologies for Environmental Control and Sustainable Development (TICASS S.c.r.l), Via Domenico Fiasella, 16121 Genoa, Italy;* [3]*Department of Architecture and Design (DAD), University of Genoa, Stradone di Sant'Agostino, 16123 Genoa, Italy*

Abstract

A 3D computational fluid dynamics model was adopted to study the effects of internal cooling on the performance of a three-fluid combined membrane contactor (3F-CMC), in the presence of minitubes in solution and a spacer in the air channel. This compact 3F-CMC is part of a hybrid climate-control system, recently developed for serving in electric vehicles. For the studied operating conditions, results show that the absorption and sensible effectiveness parameters increase up to 77% and 124% by internal cooling, respectively. This study also reports 3D flow effects on the heat and mass transfer enhancement inside the contactor, with implications for further design improvements.

Keywords: liquid desiccant; membrane contactor; internal cooling; dehumidifier; CFD

*Corresponding author. Ehsan.afrasiabian@itwm.fraunhofer.de

Received 13 February 2019; revised 11 May 2019; editorial decision 14 May 2019; accepted 14 May 2019

1 INTRODUCTION

Due to the limited energy storage capacity of electric vehicles and in order to extend their range, it is crucial to develop more energy-efficient air conditioning systems, especially for cooling and dehumidifying of hot and humid air [1, 2, 3]. Conventional vapour compression systems (VCS), which have been widely used in air conditioning, are very efficient to handle the sensible heat of air even though they suffer from inherent drawbacks. In fact, VCS cannot handle the air humidity and the latent load efficiently, especially in hot and humid climates [4]. In addition, the wet condition in such devices provides a suitable environment for mould and bacteria to grow that brings up serious health concerns and can reduce the quality of the conditioned air.

A reasonable approach to tackle these issues is to dehumidify the air by using liquid desiccants, as discussed in the literature [5, 6, 7, 8, 9]. Liquid desiccant and humid air might be in contact, without any separating media, where the moisture is directly absorbed from humid air into desiccant [10, 11]. However, this method also has some disadvantages, including desiccant droplets carry over in the handled air [12]. To prevent this issue, membrane-based dehumidifiers have been developed, where the process air and liquid desiccant are separated by means of a selective membrane [13, 14]. In these liquid–air membrane contactors, heat and water vapour transfer through the membrane while the liquid desiccant cannot pass through the pores under the operating pressures. During the vapour absorption into liquid desiccant, the condensation and dilution heats are released and liquid desiccant warms and dilutes, leading to a reduction in the dehumidification performance that could be prevented by cooling the desiccant. Thus, mainly two different approaches have been adopted to control the temperature of the desiccant within an acceptable range in membrane contactors. These are 'approach 1': applying cooling via adjacent channels [15], and 'approach 2': cooling minitubes, located inside the desiccant [16].

Several numerical studies have been carried out on the performance of two-fluid membrane contactors (2F-MC) for dehumidification (see e.g. [17, 18, 19, 20]). Furthermore, in recent years, a growing number of publications has focused on internally-cooled dehumidifiers [15, 21, 22, 23]. Even though there are some 3D computational fluid dynamics (3D-CFD) studies of the heat and mass transfer in the case of internal cooling via 'approach 1' [24], the authors are not aware of any 3D-CFD study of the heat and mass transfer in the case of internal cooling based on 'approach 2'. Let us provide some more details on the state of the art in the area. Isetti *et al.* [15] developed a three-fluid membrane contactor in

doi:10.1093/ijlct/ctz033 Advance Access publication 10 July 2019

which the refrigerant flows in cooling channels adjacent to the liquid desiccant, while air flows inside the hydrophobic membrane capillaries located in the desiccant channel. In their paper, they also established a lumped-parameter model for studying the performance of the contactor numerically. Yang *et al*. [21] adopted a mathematical model based on the effectiveness-NTU (Number of Transfer Units) method to investigate the conjugate heat and mass transfer in an adjacently-cooled membrane-based dehumidifier. Recently, Huang *et al*. [22] adopted a lumped-parameter model to describe the heat and mass transfer in a parallel plate membrane-based dehumidifier, cooled internally by means of cooling tubes inside the desiccant channel. Lately, Woods and Kozubal [23] analysed the importance of the heat and mass transfer resistance in a parallel plate three-fluid dehumidifier by means of solving partial differential equations for mass and energy balances, assuming uniform flow through each fluid channel.

Previous studies on two- and three-fluid membrane contactors have mostly focused on the operating conditions and outlet parameters, while interior heat and mass transfer was studied by few researchers [18, 24]. Thus, the effects of the local heat and mass transfer inside the dehumidifier on the absorption potential are still poorly understood. In fact, the local heat and mass transfer become more important when the simplifying assumptions are not valid anymore. For example, for flows with strong mixing and disrupted boundary layers, simplified methods using lumped-parameter or 2D models fail to predict the correct performance, and need to be adjusted by means of experiments. In this way, Huang *et al*. [18] applied Navier–Stokes equations to study the effects of developing entrances in parallel-plate ducts but in a two-fluid membrane contactor, where there was no internal cooling. Later, Huang *et al*. [24] studied conjugate heat and mass transfer in a membrane-based dehumidifier, in which water was sprayed in an adjacent channel to the desiccant and the water falling films internally cooled the solution. They solved simplified Stokes problems coupled to reduced heat and mass transfer equations. However, in the complex geometries, for instance, in the presence of cooling minitubes in the solution and spacer in the air channel, more accurate and detailed numerical approaches need to be adopted to provide not only a greater insight into the influence of internal cooling, but also the 3D flow effects on the water vapour absorption rate and dehumidification performance.

Recently, Isetti *et al*. [1, 25] proposed a three-fluid combined membrane contactor (3F-CMC) as part of a new hybrid climate-control system for electric vehicles. In this membrane contactor, humid air and liquid desiccant flow inside two separate channels so that each one is confined by two selective membranes. To control the desiccant temperature some minitubes, where the refrigerant flows, are located inside the desiccant channels. In this way, the water vapour is better absorbed by the desiccant throughout the membrane and the latent load of the absorption process is faced by this internal heat sink, namely a suitable refrigerant mass flow rate.

In addition to the internal cooling, another important factor influencing the performance of the membrane contactors is the thermal and concentration polarization in the air channels. A few experimental studies have addressed the effects of an airside spacer on the performance of membrane contactor dehumidifiers [26]; however, due to the complex flow patterns, it has been neglected in the numerical investigations and the 3D effects remained poorly visualized and understood.

In this paper, a comprehensive fully 3D-CFD model is used to investigate the effect of internal cooling on the absorption potential of a 3F-CMC where a spacer is present in the air channel, and cooling is achieved by means of minitubes in the solution, and to compare it with the respective 2F-MC. This 3F-CMC was recently proposed by Isetti *et al*. [1, 25]. Moreover, the 3D flow effects of the 3F-CMC design on the concentration and thermal polarization phenomena are reported to deepen our understanding of the heat and mass transfer inside the membrane contactor, which will pave the way for further developments.

1.1 Description of the 3F-CMC

A small-scaled prototype and a computer-aided engineering (CAE) design of the considered 3F-CMC are shown in Figures 1 and 2. The current unit consists of 11 repetitive elements, which are assembled to form the 3F-CMC. The prototype of the 3F-CMC, depicted in Figure 1, is designed to treat 70 $\left(m^3hr^{-1}\right)$ of external air with an air pressure drop lower than 100 (Pa); the prototype volume is $V = 6.6\ \left(dm^3\right)$, with a ratio between active membrane surface and volume equal to $R = 100\ m^{-1}$. The prototype's compactness can still be enhanced, thus further easing its installation on board of electric vehicles that are now on the market. Figure 2 also depicts a magnified section of some repetitive elements, showing the membranes (in red), spacer (in green), frame (in blue) and minitubes (in grey). In the current device, the spacer plays an important role in supporting the membrane to prevent its deflection and in enhancing the heat and mass transfer by increasing the airflow mixing along the air channel. Two adjacent frames with all components inside (membranes, minitubes and sealing gaskets) and one spacer form the repetitive element of the 3F-CMC. As Figure 2 shows, different flow domains can be distinguished: the channels for air, given by the spacer and membranes, and the domain for desiccant, on the outside of minitubes and confined by the membranes. In detail, humid air flows inside the air channels crossing the spacer, while the liquid desiccant flows in the orthogonal direction between the membranes and the minitubes. In the minitubes lumina the refrigerant flows to cool the desiccant; the refrigerant and desiccant flows have co/counter current arrangement, transversal to the humid airflow direction.

1.2 Numerical model

Since the whole process in the absorption dehumidification is complicated, the steady state flow is considered and the following simplifying assumptions are adopted:

- Water vapour condenses at the wetted membrane surface in the desiccant channel;
- Both humid air and solution flows are laminar and incompressible;

Figure 1. *The prototype of the 3F-CMC (two views).*

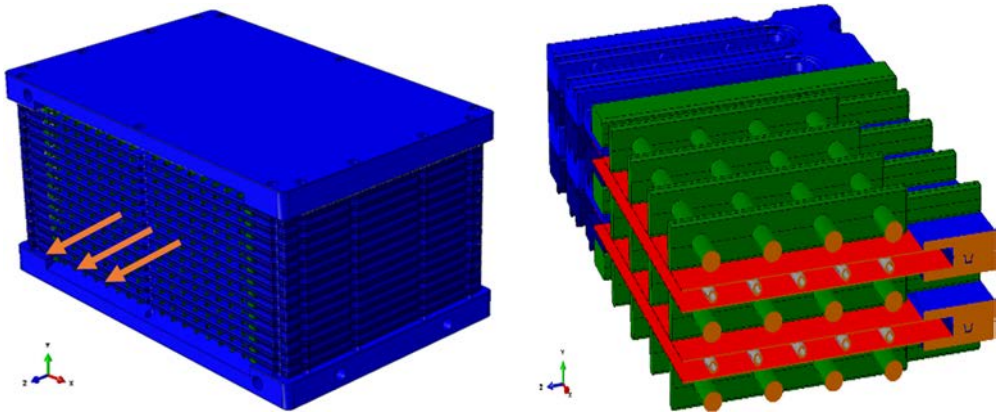

Figure 2. *(Left) CAE design of the 3F-CMC (vectors illustrate the airflow direction through the device) and (right) A magnified section of the CAE design, illustrating the air and solution channels, spacer (in green), minitubes (in grey) and membranes (in red).*

- Neither vapour condensation at the airside nor salt crystallization at the desiccant side of the membrane are considered.

In the current work, half of one repetitive module is modelled, including the spacer, minitubes, air and desiccant channels with one membrane in between. For each phase (i.e. humid air and LiCl solution), the following governing equations have to be solved:

Continuity:

$$\nabla \cdot \left(\rho_j \overrightarrow{u}_j\right) = S_{m,j} \tag{1}$$

Momentum:

$$\nabla \cdot \left(\rho_j \overrightarrow{u}_j \overrightarrow{u}_j\right) = -\nabla p_j + \nabla \cdot \overline{\overline{\tau_j}} \tag{2}$$

Energy:

$$\nabla \cdot \left(\rho_j \overrightarrow{u}_j h_j\right) = \overline{\overline{\tau_j}} : \nabla \overrightarrow{u}_j - \nabla \left(k_j \nabla T\right) + S_{h,j} \tag{3}$$

Here $j \in \{a, d\}$, and the stress tensor reads as:

$$\overline{\overline{\tau_j}} = \mu_j \left[\left(\nabla \overrightarrow{u_j} + \nabla \overrightarrow{u_j}^T\right) - \frac{2}{3} \nabla \cdot \overrightarrow{u_j} I\right].$$

One transport equation is solved for the mass fraction of water vapour $\left(c_v = m_v / m_{da}\right)$ in humid air.

$$\nabla \cdot \left(\rho_a \overrightarrow{u}_a c_v - \rho_a D_{v-a} \nabla c_v\right) = S_v \tag{4}$$

After water vapour passes through the membrane condenses into liquid water, which dilutes the desiccant. Thus, one transport equation is also solved for the mass fraction of the condensed water ($c_{cw} = m_{cw} / m_{d,i}$) in the liquid desiccant, reading as

$$\nabla \cdot \left(\rho_d \overrightarrow{u}_d c_{cw} - \rho_d D_{cw-d} \nabla c_{cw}\right) = S_{cw} \tag{5}$$

Since both flows are dilute for the vapour and condensed water, the 'constant dilute approximation' for the diffusivity (D) is applied in this study.

In this numerical approach, heat and mass transfer between different phases are coupled by setting proper source terms, added to the governing equations. These source terms are based on the vapour mass flux rate $\dot{m}_{sur}\left(kg\ m^{-2}\ s^{-1}\right)$ through the membrane, which are non-zero in the very first layer of cells in the desiccant domain, adjacent to the membrane. In the adopted finite volume-based method, source and sink terms are defined based on the

mass transfer rate per unit volume, $\dot{m}_{vol}\left(kg\,m^{-3}s^{-1}\right)$ then one can write

$$\int_{V_{cell}} \dot{m}_{vol} dV = \int_{A_{cell}} \dot{m}_{sur} dA \rightarrow \dot{m}_{vol} = \frac{A_{cell}}{V_{cell}} \dot{m}_{sur} \quad (6)$$

Here V_{cell} represents the cell volume of the meshes in which mass transfer takes place, and A_{cell} is the corresponding surface of these cells attached to the membrane surface.

Furthermore, due to the water vapour diffusion through the membrane, followed by condensation, the latent heat of condensation and dilution are released on the desiccant side. In the current study and for the considered range of LiCl mass fraction, the heat of dilution is deemed negligible compared to the heat of condensation and the source terms read as

$$S_{m,d} = \dot{m}_{vol} \quad (7)$$

$$\begin{aligned} S_{h,d} &= \dot{m}_{vol}\left(h_l + c_p\left(T - T_0\right)\right) \\ S_{h,a} &= -\dot{m}_{vol} c_p\left(T - T_0\right) \end{aligned} \quad (8)$$

$$\begin{aligned} S_v &= -\dot{m}_{vol} \\ S_{sw} &= \dot{m}_{vol} \end{aligned} \quad (9)$$

1.3 At the membrane

The membrane is modelled as a solid wall that separates the desiccant and humid air flows, while the heat and mass flux, normal to the membrane surface (y-direction), are conserved.

$$\begin{aligned} \frac{\partial^2 T_{mem}}{\partial y^2} &= 0 \\ \frac{\partial \dot{m}}{\partial y} &= 0 \end{aligned} \quad (10)$$

At the desiccant side of the membrane where absorption takes place, the equilibrium partial pressure (PP) of water vapour reduces, while on the other side of the membrane, the (PP) of water vapour is higher. This difference in the (PP) of the vapour drives water molecules through the microstructure of the membrane [15]. Thus, the mass flux rate of water vapour is

$$\dot{m}_{sur} = K_v\left(p_{va} - p_{vd}\right). \quad (11)$$

Here K_v is the mass transfer resistance coefficient, p_{va} is the (PP) of the vapour in the air, and p_{vd} is the equilibrium (PP) of the water vapour at the interface of air/desiccant. Conde-Petit [27] proposed the following relations for the equilibrium (PP) of water vapour for LiCl solution

$$p_{vd}\left(T, x\right) = p_{sv}\pi_{25}\left(A + B\theta\right), \quad (12)$$

where the saturation pressure for water vapour reads as

$$p_{sv}(T) = 610.94 \times \exp\left(\frac{17.625\left(T - 273.15\right)}{\left(T - 273.15\right) + 243.04}\right) \quad (13)$$

and

$$\pi_{25}(x) = 1 - 0.03\exp\left(-\frac{(x-0.1)^2}{0.005}\right) - \left(\left(\frac{x}{0.362}\right)^{-4.75} + 1\right)^{-0.4} \quad (14)$$

$$A(x) = 2 - \left(\left(\frac{x}{0.28}\right)^{4.3} + 1\right)^{0.6} \quad (15)$$

$$B(x) = \left(\left(\frac{x}{0.21}\right)^{5.1} + 1\right)^{0.49} - 1 \quad (16)$$

$$\theta(T) = \frac{T}{647.096}. \quad (17)$$

In Equations (14–16) the salt concentration is

$$x = \frac{m_{LiCl}}{m_d + m_{cw}}. \quad (18)$$

1.4 Boundary conditions

In this study, the spacer is modelled as a solid zone where heat is conducted, coupled with the convective heat transfer in humid air. The inlet and outlet boundary conditions, for both desiccant and humid air, are velocity-inlet and pressure-outlet, respectively. The minitubes are assumed adiabatic with Neumann boundary condition in the 2F-MC case, while in the 3F-CMC are set to a constant temperature to account for the changing-phase refrigerant. All the other boundary conditions and the simulation process for both cases are the same. The membrane is reduced to a thin solid wall where the heat is conducted through it, coupled with the fluid zones on both its sides.

1.5 Solution scheme

In the present study, ANSYS-Fluent (v.18.1) was used to investigate the conjugate heat and mass transfer in the 3F-CMC. The absorption process was modelled by developing proper user-defined functions and scalars. To describe the humid air, the Species model was used with weighted-average properties of dry air and water vapour. The velocity and pressure coupling was achieved by Coupled algorithm. Mesh dependency was examined and 9.2×10^6 hexahedral cells were chosen for the computational domain. The criterion for the convergence is when the residuals drop below 10^{-7}.

Table 1. *Operating parameters reported in [28].*

EXP.NO.	$\dot{m}_a$ $(kg\ hr^{-1})$	$\dot{m}_d$ $(kg\ hr^{-1})$	$c_{v,i}$ $\left(g\ kg_{da}^{-1}\right)$	x_i (%)
1	*5.29*	*8.31*	*14.3*	*32.1*
2	*5.31*	*8.36*	*20.2*	*32.0*
3	*5.32*	*12.46*	*14.2*	*32.1*
4	*5.32*	*8.47*	*14.2*	*37.0*

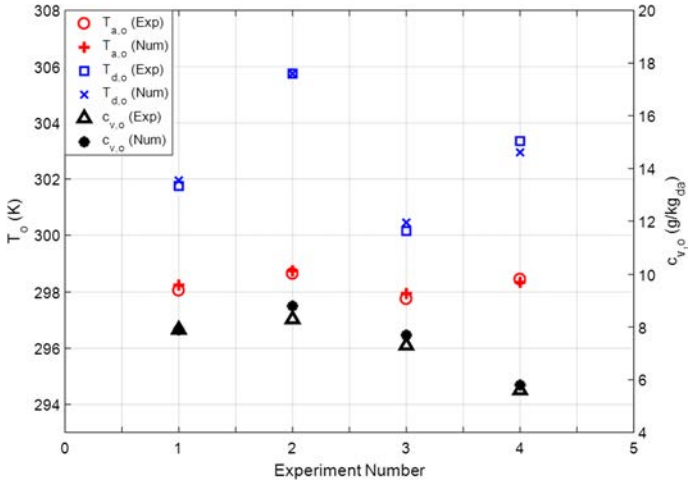

Figure 3. *Current numerical results vs. experimental data reported in [28].*

2 RESULTS AND DISCUSSIONS

2.1 Validation

First, the numerical model for conjugate heat and mass transfer through a selective membrane is validated using the experimental data for a simpler case of a 2F-MC, reported in [28]. In [28], the authors investigated the influence of different inlet conditions on the performance of a small-scale single-panel liquid-to-air contactor, in which moisture is absorbed from humid air into LiCl solution through a selective membrane. Table 1 presents different test conditions reported in [28] where the temperature of the inlet air and desiccant are 297.15 (K) and 303.15 (K), respectively. Figure 3 compares the experimental data emerged from their tests and the numerical results from the current CFD simulation. Here, the mass transfer resistance coefficient $\left(K_v\right)$ is obtained by fitting the numerical data with the first experiment, indicated as 'EXP. No. 1' in Table 1. Then, the obtained coefficient for K_v was applied to other cases and, as Figure 3 shows, the numerical results for the outlet temperatures and humidity agree well with the published experimental data under different operating conditions.

2.2 Simulation of the 3F-CMC

The dehumidification process inside the 3F-CMC was modelled and compared with respective 2F-MC (same device with no refrigerant involved) to investigate the effects of internal cooling on the water vapour absorption. In the simulations, based on the foreseen operating conditions, the LiCl solution enters the desiccant channel in the computational domain at $x_i = 0.255$ with $\dot{m}_d = 0.88\ \left(kg\ hr^{-1}\right)$, and $T_{d,i} = 290.25\ (K)$. The humid air enters the air channel with $\dot{m}_a = 3.23\ \left(kg\ hr^{-1}\right)$and $T_{a,i} = 303.65\ (K)$, while the relative humidity is 63%$\left(c_v = 17.4\ g\ kg_{da}^{-1}\right)$. In the 3F-CMC where the desiccant solution is cooled internally, the minitubes temperature (T_{ref}) is 288.25 (K). The thermo-physical properties of the spacer, membrane and LiCl solution used in the simulation are summarized in Table 2.

Table 2. *Spacer, membrane and desiccant properties.*

Parameter	Value	Parameter	Value
$\rho_s\left(kg\ m^{-3}\right)$	1555	$c_{p_s}\left(J\ kg^{-1}\ K^{-1}\right)$	1400
ρ_{mem}	1320	$c_{p_{mem}}$	970
ρ_d	1150	c_{p_d}	3100
$k_s\left(W\ m^{-1}\ K^{-1}\right)$	0.49	$K_v\left(s\ m^{-1}\right)$	1.4×10^{-7}
k_{mem}	0.16	$\delta_{mem}(mm)$	0.165
k_d	0.52	$D_{cw-d}\left(m\ s^{-1}\right)$	1.38×10^{-9}

To investigate the performance of the contactor, two effectiveness parameters are introduced as the absorption effectiveness (ε_{ab}) and sensible effectiveness(ε_{se}). In this paper, ε_{ab} and ε_{se} are respectively defined as the ratio of the actual removed moisture and reduced temperature of humid air to the maximum possible values in the reference case, i.e. the ideal case where both the temperature and concentration of desiccant are considered constant and equal to their inlet values. Then, the effectiveness parameters read as [29]

$$\varepsilon_{ab} = \frac{c_{v,i} - c_{v,o}}{c_{v,i} - c_{d,i}} \tag{19}$$

$$\varepsilon_{se} = \frac{T_{a,i} - T_{a,o}}{T_{a,i} - T_{d,i}}, \tag{20}$$

where $c_{d,i}$ is the equilibrium water vapour content at the interface between air and inlet liquid desiccant, defined as

$$c_{d,i} = 0.622 \frac{p_{vd,i}}{p_i - p_{vd.i}}. \tag{21}$$

In Figures 4–7 humid air enters from the bottom and the desiccant flows from the right to the left, separated by the membrane (see Figure 4). As Figure 4 shows, there is a significant difference in the temperature fields at the membrane between two cases (3F-CMC and 2F-MC). In the 2F-MC (left), a gradual increase in the temperature of the desiccant at the membrane is seen. On the contrary, it is apparent that for 3F-CMC (right) the temperature distribution on the membrane is largely affected by the refrigerant temperature, especially above the minitubes. This figure shows how the internal cooling successfully restrains the desiccant temperature within a significantly narrow range.

Figure 5 shows the effects of the temperature on the vapour equilibrium (PP) at the desiccant side and Figure 6 illustrates the

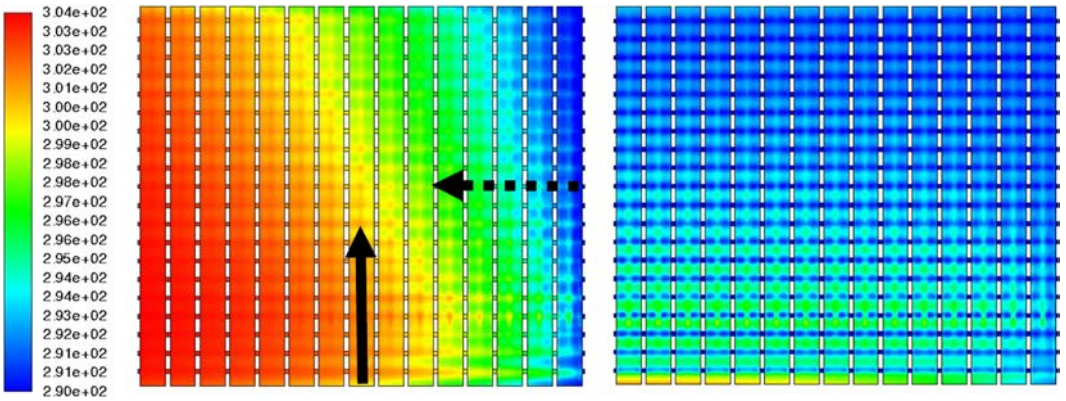

Figure 4. *Temperature distribution (K) at the membrane (airside) and minitubes for the 2F-MC (left) and 3F-CMC (right). Dashed and solid arrows indicate the desiccant and airflow directions, respectively.*

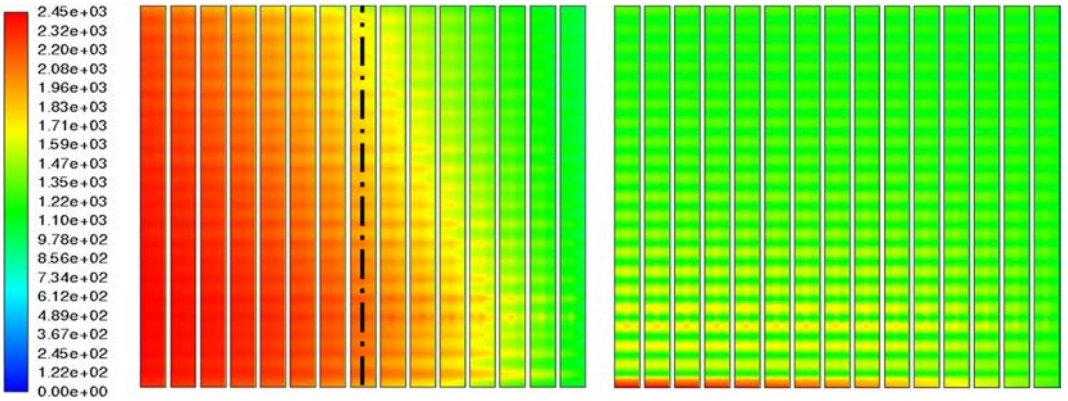

Figure 5. *Water vapour equilibrium (PP) at the membrane (desiccant side) for the 2F-MC (left) and 3F-CMC (right). Dashed line illustrates the location of the longitudinal cross-section.*

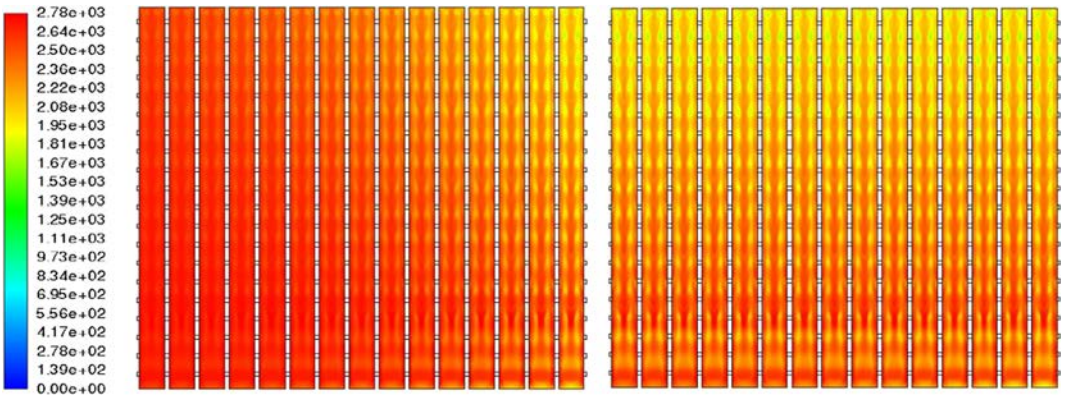

Figure 6. *(PP) of water vapour at the membrane (airside) for the 2F-MC (left) and 3F-CMC (right).*

water vapour (PP) at the airside of the membrane. From Figures 5 and 6 it follows that in the 2F-MC, by increasing the temperature the equilibrium (PP) at the desiccant side of the membrane is continuously increasing, while the absorption potential decreases. It makes the major part of the membrane surface less effective, in terms of water vapour absorption, compared to the entrance region. On the contrary, for the 3F-CMC, the water vapour pressure difference and the overall mass transfer potential at the wetted membrane surface is higher. In this way, the driving force for the moisture transport through the membrane does not drop and is almost constant along the desiccant flow direction, leading to a higher absorption rate compared to the 2F-MC.

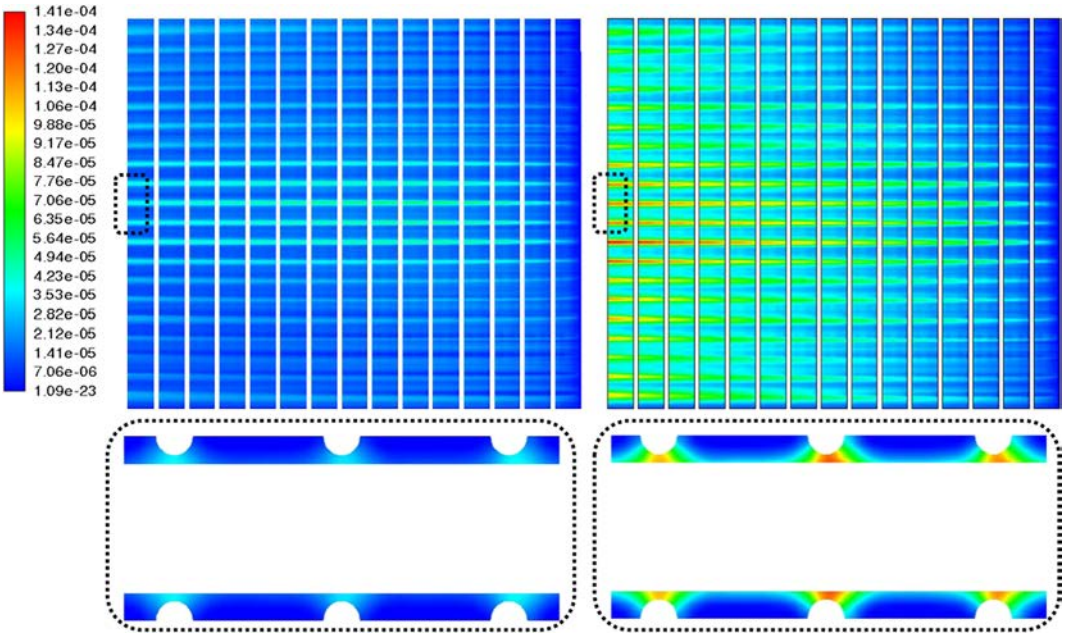

Figure 7. *Mass fraction of the condensed water,* $c_{cw}\left(kg\ kg_{d,i}^{-1}\right)$*, for 2F-MC (left) and 3F-CMC (right); (top) at the membrane (desiccant side) and (bottom) at the magnified section of the outlet.*

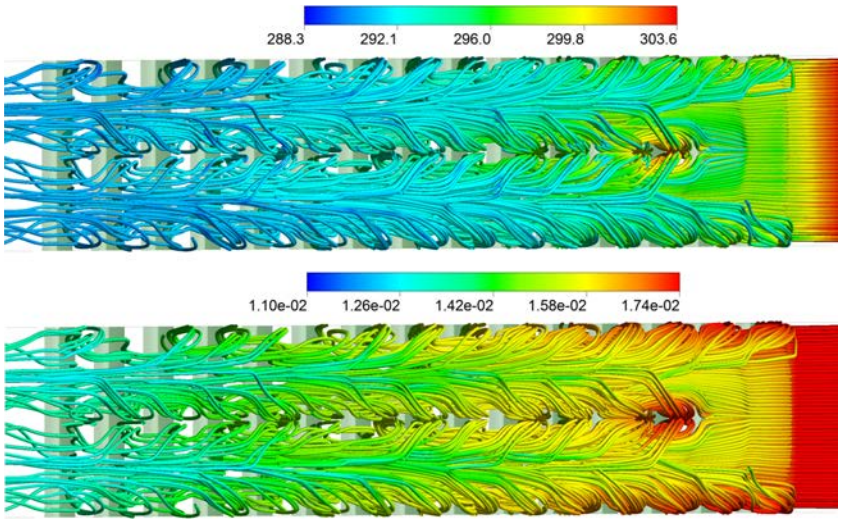

Figure 8. *Air flow streamlines through one air passage coloured by (top) air temperature* $\left(K\right)$ *and (bottom) water vapour mass fraction* $\left(kg\ kg_{da}^{-1}\right)$.

Furthermore, Figure 7 compares the distributions of the mass fraction of the condensed water $\left(c_{cw}\right)$ at two sections: (top) at the desiccant side of the membrane, and (bottom) at the outlet of the desiccant channel. This distribution is due to the mass transfer from humid air to the liquid desiccant, which is convected and diffused through the liquid desiccant. It is evident that the amount of the condensed water in the 3F-CMC is remarkably higher than 2F-MC.

Figure 7 (bottom) shows the distribution of mass fraction of the condensed water at the outlet cross-section, normal to the desiccant flow direction. Evidently, there is higher concentration of the condensed water on top of the minitubes. This phenomenon might be explained by the low-temperature and low-velocity zones, right above the minitubes. This concentration gradient, known as concentration polarization, is reported in different membrane-based separation processes for liquid and gas feed flows [30, 31]. This figure implies how the temperature and velocity of the desiccant can affect the local moisture absorption.

Additionally, the considered 3F-CMC could be distinguished from available membrane contactors due to the particular design of the spacer. One main role of the spacer in the 3F-CMC is

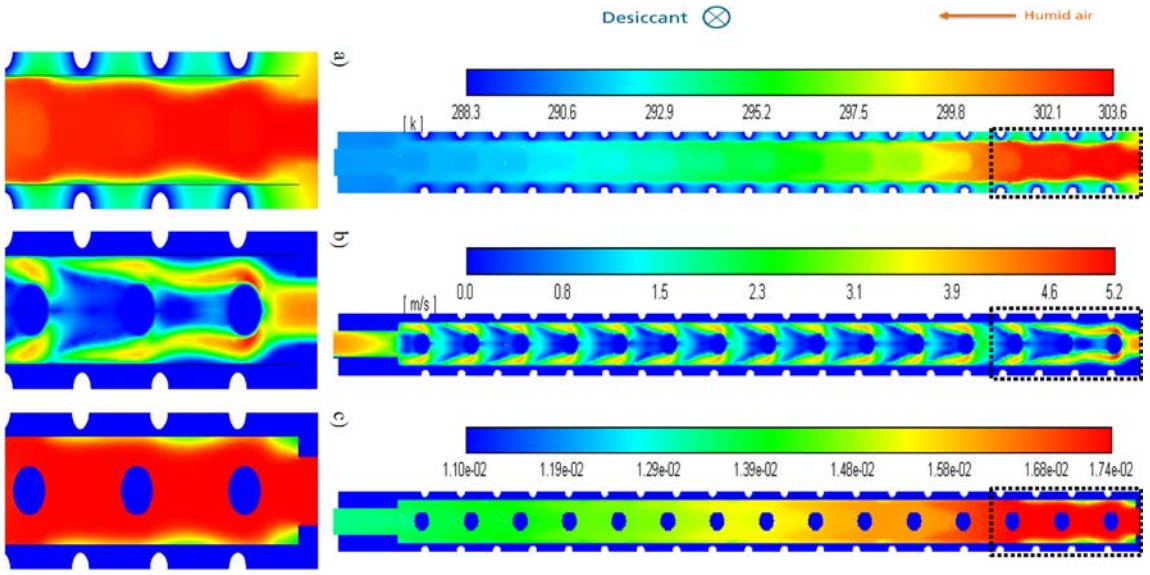

Figure 9. *(**a**) Temperature (K), (**b**) velocity* $\left(m\ s^{-1}\right)$ *and (**c**) vapour mass fraction* $\left(kg\ kg_{da}^{-1}\right)$ *contours in the 3F-CMC (magnified sections are shown at bottom).*

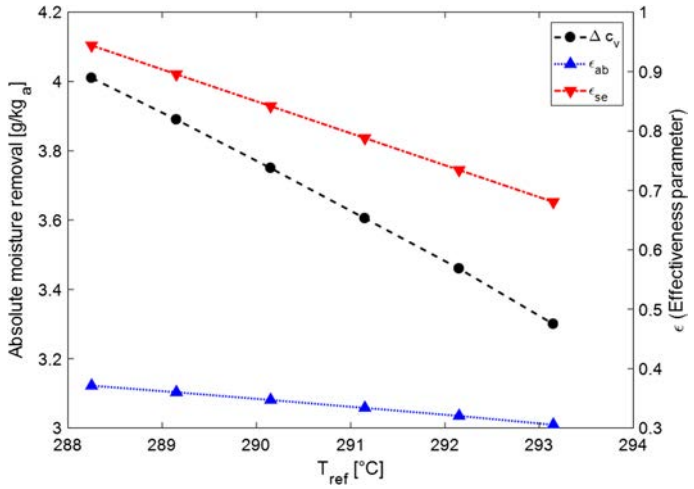

Figure 10. *Effects of the temperature of the refrigerant on the absolute moisture removal, absorption and sensible effectiveness parameters.*

to enhance heat and mass transfer by increasing the mixing and decreasing the polarization phenomena. Numerical results from the current CFD simulation predict a proper functionality of the spacer to meet this purpose. Figure 8 illustrates the streamlines of the inlet airflow through one air channel (in the views shown in Figures 8 and 9 air flows from right to left). These streamlines show how water vapour mass fraction$\left(c_v\right)$ and temperature (T) undergo changes between the inlet and outlet. As these streamlines indicate, the spacer induces mixing in the air channel. Figure 9 depicts the distributions of the corresponding temperature, velocity and specific humidity in a longitudinal cross-section of the 3F-CMC, perpendicular to the desiccant/refrigerant flows as shown in Figure 5 (with dashed line). As it is implied by Figure 8(top) and supported by Figure 9(a) (in 2D view), due to these 3D effects caused by the spacer, the thermal boundary layer at the membrane is disrupted, which leads to the heat transfer enhancement. These 3D effects on the flow boundary layer are also evident in Figure 9(b), where the velocity contour (in 2D view) is illustrated. Similarly, the same mechanism is seen in Figure 8(bottom) and Figure 9(c) for the mass fraction of water vapour in humid air, which is linked to the water vapour (PP). Indeed, due to the moisture absorption, along the air stream, the water vapour content in the humid air reduces and a low vapour concentration boundary layer starts forming and growing at the membrane sheet, which is disrupted and broken by the airflow mixing. In this way, the concentration polarization on the airside (feed side) of the membrane reduces, leading to a higher driving force for the water vapour absorption through the membrane. Thanks to the spacer design, this phenomenon enhances the dehumidification and absorption effectiveness of the device.

Moreover, the performance of the 3F-CMC was investigated for different refrigerant temperatures and was compared with the respective 2F-MC (no internal cooling). As Figure 10 demonstrates, the minitubes´ temperature has a remarkable influence on the absolute moisture removal and effectiveness parameters compared to the 2F-MC case. According to the numerical results, when the refrigerant temperature is 293.15 K, the absolute moisture removal in the 3F-CMC is 47% higher compared to that of the 2F-MC. By decreasing the refrigerant temperature to 288.25 K, leading to a stronger internal cooling, this enhancement rises to ∼79%. This shows how internal cooling promotes the absorption rate in the current 3F-CMC, by raising the affinity of the desiccant for the water vapour.

As Figure 10 illustrates, the 3F-CMC also treats the sensible load more effectively than the 2F-MC. As numerical results demonstrate, the sensible effectiveness parameter in the 3F-CMC

increased from 0.68 to 0.94 when refrigerant temperature decreased from 293.15 to 288.25 that are respectively 62% and 124% higher than that of the 2F-MC. Likewise, these values for the absorption effectiveness parameter ranged from 47% to 77%. These imply that in the 3F-CMC both streams at the outlets are partially cooled, and the absorption rate is enhanced accordingly. Based on the above discussion the lower refrigerant temperature results in the higher absorption rate in the 3F-CMC.

3 CONCLUSION

In the present paper, we studied the conjugate heat and mass transfer inside a membrane-based dehumidifier, called 3F-CMC, designed for serving in a hybrid climate-control system for electric vehicles. A fully 3D-CFD model was adopted to study the effects of internal cooling in a compact membrane contactor for liquid desiccant dehumidification, where the minitubes and spacer are presented in the desiccant and air channels, respectively. The applied numerical method provides detailed information to understand the flows´ complex behaviour and absorption potential inside the device. The results of this investigation showed that the current spacer design of the 3F-CMC has a significant impact on the heat and mass transfer enhancement by disrupting water vapour concentration and thermal boundary layers. Moreover, this study showed that internal cooling has an important impact on the moisture absorption rate and the sensible load facing. As numerical results indicated, the absolute moisture removal in the internally-cooled contactor (3F-CMC), when $288.25 < T_{ref} < 293.15\ K$, is between 47% and 79% higher than the respective 2F-MC, which works without the refrigerant. Likewise, the sensible effectiveness parameter increased from 0.42 in the 2F-MC to the value between 0.68 and 0.94 in the 3F-CMC, in the considered range of refrigerant temperatures. Taken together, these findings deepen our understanding of how dehumidification takes place in complex geometries along with implications for the future optimization of the membrane-based dehumidifiers.

ACKNOWLEDGMENTS

This work is part of XERIC project that has received funding from the European Union's Horizon 2020 research and innovation programme under grant agreement N°653605.

REFERENCES

[1] Isetti C, Nannei E, Lazzari S *et al.* 2017. New climate-control units for more energy-efficient electric vehicles: the innovative three-fluids combined membrane contactor. In *2017 Twelfth International Conference on Ecological Vehicles and Renewable Energies (EVER)*. Monaco, April 2017.

[2] Zhang L, Hashimoto K, Hasegawa H *et al.* Performance analysis of a heat pump system with integrated desiccant for electric vehicles. *Int J Refrig* 2018;**86**:154–62.

[3] Qi Z. Advances on air conditioning and heat pump system in electric vehicles—a review. *Renew Sustain Energy Rev* 2014;**38**:754–64.

[4] Dai YJ, Wang RZ, Zhang HF *et al.* Use of liquid desiccant cooling to improve the performance of vapor compression air conditioning. *Appl Therm Eng* 2001;**21**:1185–202.

[5] Kinsara AA, Elsayed MM, Al-Rabghi OM. Proposed energy-efficient air-conditioning system using liquid desiccant. *Appl Therm Eng* 1996; **16**:791–806.

[6] Labban O, Chen T, Ghoniem AF *et al.* Next-generation HVAC: Prospects for and limitations of desiccant and membrane-based dehumidification and cooling. *Appl Energy* 2017;**200**:330–46.

[7] Keniar K, Ghali K, Ghaddar N. Study of solar regenerated membrane desiccant system to control humidity and decrease energy consumption in office spaces. *Appl Energy* 2015;**138**:121–32.

[8] Zhang N, Yin SY, Zhang LZ. Performance study of a heat pump driven and hollow fiber membrane-based two-stage liquid desiccant air dehumidification system. *Appl Energy* 2016;**179**:727–37.

[9] Abdel-Salam MR, Fauchoux M, Ge G *et al.* Expected energy and economic benefits, and environmental impacts for liquid-to-air membrane energy exchangers (LAMEEs) in HVAC systems: a review. *Appl Energy* 2014;**127**:202–18.

[10] Radhwan AM, Gari HN, Elsayed MM. Parametric study of a packed bed dehumidifier/regenerator using CaCl2 liquid desiccant. *Renew Energy* 1993;**3**:49–60.

[11] Islam MR, Alan SWL, Chua KJ. Studying the heat and mass transfer process of liquid desiccant for dehumidification and cooling. *Appl Energy* 2018;**221**:334–47.

[12] Rane MV, Reddy SVK, Easow RR. Energy efficient liquid desiccant-based dryer. *Appl Therm Eng* 2005;**25**:769–81.

[13] Isetti C, Nannei E, Magrini A. On the application of a membrane air—liquid contactor for air dehumidification. *Energ Buildings* 1997;**25**:185–93.

[14] Zhang LZ, Jiang Y. Heat and mass transfer in a membrane-based energy recovery ventilator. *J Membr Sci* 1999;**163**:29–38.

[15] Isetti C, Nannei E, Orlandini B. Three-fluid membrane contactors for improving the energy efficiency of refrigeration and air-handling systems. *Int J Ambient Energy* 2013;**34**:181–94.

[16] Abdel-Salam MR, Besant RW, Simonson CJ. Design and testing of a novel 3-fluid liquid-to-air membrane energy exchanger (3-fluid LAMEE). *Int J Heat Mass Transf* 2016;**92**:312–29.

[17] Bai H, Zhu J, Chen Z *et al.* Parametric analysis of a cross-flow membrane-based parallel-plate liquid desiccant dehumidification system: numerical and experimental data. *Energ Buildings* 2018;**158**:494–508.

[18] Huang SM, Zhang LZ, Yang M. Conjugate heat and mass transfer in membrane parallel-plates ducts for liquid desiccant air dehumidification: effects of the developing entrances. *J Membr Sci* 2013;**437**:82–9.

[19] Sabek S, Nasr KB, Tiss F *et al.* Performance investigation of desiccant liquid air membrane energy exchanger: Air and lithium chloride effects. *Int J Refr* 2017;**80**:145–57.

[20] Das RS, Jain S. Performance characteristics of cross-flow membrane contactors for liquid desiccant systems. *Appl Energy* 2015;**141**:1–11.

[21] Yang Y, Yang M, Huang W *et al.* Heat and mass transfer in an adjacent internally-cooled membrane-based liquid desiccant dehumidifier (AIMLDD). *Energy Procedia* 2017;**142**:3990–7.

[22] Huang SM, Yang M, Hu B *et al.* Performance analysis of an internally-cooled plate membrane liquid desiccant dehumidifier (IMLDD): an analytical solution approach. *Int J Heat Mass Transf* 2018;**119**: 577–85.

[23] Woods J, Kozubal E. On the importance of the heat and mass transfer resistances in internally-cooled liquid desiccant dehumidifiers and regenerators. *Int J Heat Mass Transf* 2018;**122**:324–40.

[24] Huang SM, Zhong Z, Yang M. Conjugate heat and mass transfer in an internally-cooled membrane-based liquid desiccant dehumidifier (IMLDD). *J Membr Sci* 2016;**508**:73–83.

[25] Isetti C, Nannei E, Lazzari S *et al.* XERIC climate-control system for energy-efficient electric vehicles: first experimental results and numerical

evaluation of the overall performance. In *Thirteenth International Conference on Ecological Vehicles and Renewable Energies (EVER)*, 2018, April, p. 1–6. Monte-Carlo, Monaco.

[26] Moghaddam DG, Oghabi A, Ge G *et al.* Numerical model of a small-scale liquid-to-air membrane energy exchanger: parametric study of membrane resistance and air side convective heat transfer coefficient. *Appl Therm Eng* 2013;**61**:245–58.

[27] Conde-Petit MR. Aqueous solution of lithium and calcium chlorides: property formulations for use in air conditioning equipment design. *Zurich, Switzerland*, 2014.

[28] Ge G, Moghaddam DG, Abdel-Salam AH *et al.* Comparison of experimental data and a model for heat and mass transfer performance of a liquid-to-air membrane energy exchanger (LAMEE) when used for air dehumidification and salt solution regeneration. *Int J Heat Mass Transf* 2014;**68**:119–31.

[29] Qi R, Lu L, Yang H. Development of simplified prediction model for internally cooled/heated liquid desiccant dehumidification system. *Energ Buildings* 2013;**59**:133–42.

[30] Bui TD, Wong Y, Islam MR *et al.* On the theoretical and experimental energy efficiency analyses of a vacuumbased dehumidification membrane. *J Membr Sci* 2017;**539**:76–87.

[31] Calo VM, Iliev O, Nunes SP. Cell-element simulations to optimize the performance of osmotic processes in porous membranes. *Comput Math Appl* 2018;**76**:361–76.